applied sciences

MDPI

Article

Evaluating the Impact of Seismic Activity on the Slope Stability of the Western Coast of Lefkada Island Using Remote Sensing Techniques, Geographical Information Systems, and Field Data

Konstantinos G. Nikolakopoulos *, Ioannis K. Koukouvelas, Aggeliki Kyriou, Dionysios Apostolopoulos and George Pappas

Department of Geology, University of Patras, 265 04 Patras, Greece; ioannis@upatras.gr (I.K.K.); a.kyriou@upnet.gr (A.K.); apostolopoulos.dionysios@upatras.gr (D.A.); up1048086@upnet.gr (G.P.)
* Correspondence: knikolakop@upatras.gr

Abstract: The current research aims to examine the long-term evolution of the western cliffs of Lefkada Island following the occurrence of the last two strong earthquakes, on 14 August 2003 and 17 November 2015, respectively. Medium resolution satellite data (Landsat) and very high-resolution data (Ikonos, Pleiades, and airphotos) were processed in Google Earth Engine and Erdas imagine software, respectively. The study area covers a 20 km-long region of the western cliffs of Lefkada Island, extending from Egremni beach to the South to Komilio beach to the North. Relief, vegetation, and inclination changes were detected in the ArcGis environment. The results were associated with in situ data provided through the installation of a sediment trap. The analysis of the results proved that seismicity is the main factor that formed the western coastline of Lefkada Island, affecting the integrity of the cliffs. Specifically, large earthquakes cause immediate vegetation and topographic (inclination changes, mass movements) modifications in the western cliffs of the island. Meanwhile, small earthquakes (magnitudes < 4.1) contribute to the cliff's evolution during the inter-seismic era. The intensity of these aforementioned changes was closely related to the seismic activity that occurred in the vicinity of the study area. In addition, it was found that precipitation and wind do not exert a similar influence on the cliff's evolution.

Keywords: slope analysis; seismicity; remote sensing; geomorphological analysis; Lefkada coast

Citation: Nikolakopoulos, K.G.; Koukouvelas, I.K.; Kyriou, A.; Apostolopoulos, D.; Pappas, G. Evaluating the Impact of Seismic Activity on the Slope Stability of the Western Coast of Lefkada Island Using Remote Sensing Techniques, Geographical Information Systems, and Field Data. *Appl. Sci.* **2023**, *13*, 9434. https://doi.org/10.3390/app13169434

Academic Editor: John Dodson

Received: 26 July 2023
Revised: 4 August 2023
Accepted: 10 August 2023
Published: 20 August 2023

1. Introduction

The evolution of the relief in seismically and tectonically active regions is dominated by the occurrence of earthquakes. These events contribute to the destabilization of the slope, triggering topographic changes or landslides. Earthquake-induced mass movements can cause casualties, economic loss, and severe damages to the natural and man-made environment [1,2]. Over the past few years, extensive studies have been performed on determining the parameters of earthquake-induced landslides either through laboratory simulations and numerical modeling [3–6] or by investigating the instability factors, the distribution of mass movements, and the topography [7,8]. In this framework, remote sensing enables the effective detection and monitoring of landslides on either a local or regional scale due to the large-area observations and the reduced survey completion time. Hence, multispectral (Landsat, WorldView-2, GeoEye-1, etc.), as well as synthetic aperture radar (SAR) (TerraSAR-X, COSMO-SkyMed, ALOS-2 PALSAR-2, Sentinel-1), data have been used for the identification and analysis of landslides with high precision [9–12]. Nowadays, unmanned aerial systems (UAS) photogrammetry constitutes the most widely used method for landslide investigations [13–15].

As technology and processing methods develop, new approaches are emerging, relying on soft computing algorithms in order to detect earthquake-induced landslides or create susceptibility maps. Specifically, an automated methodology was proposed to map

co-seismic landslides. Its methodology was based on multi-scale extended morphological profiles, machine learning algorithms, and unsupervised change detection methods [16]. Moreover, high-resolution images, acquired using Planet satellite, were utilized for the detection of landslides after the Mw6.6 Tomakomai earthquake, while the extracted inventory database was used to generate susceptibility maps via logistic regression and support vector machine modeling [17]. In a respective study, the importance of inventory quality was highlighted by examining different databases of earthquake-induced landslides to create susceptibility models for a given area [18]. Other researchers have investigated how multiple susceptibility algorithms affect the prediction of landslides related to the Hokkaido earthquake [19].

However, the majority of these previous studies mainly focused on either the instantaneous mapping of earthquake-induced topographic changes or on the creation of landslide susceptibility over tectonically active regions [12,15–19]. Despite the immediate effects of an earthquake on a slope, there are areas that, while they do not move, have a disturbed internal structure, and they can be activated by smaller earthquakes or other external factors, such as rainfall [5]. In light of this, this study aimed to examine the long-term evolution of the western cliffs of Lefkada Island following the occurrence of the last two strong earthquakes, on 14 August 2003 and 17 November 2015, respectively.

Specifically, we obtained multi-sensor remote sensing data, covering a period from the years 2000 to 2016, to investigate the evolution of the western cliffs of Lefkada Island after the occurrence of the last strong earthquakes as well as during the inter-seismic era. It is worth mentioning that previous studies have been conducted on inspecting shoreline evolution over a 73-year period using diverse remote sensing data [20] and assessing the evolution of mass movements between 2018–2021 through field measurements and unmanned aerial vehicle (UAV) campaigns [21]. However, the main objective of the current research was to determine the factors (seismicity and precipitation) that reduce the integrity of the cliffs in the western part of Lefkada Island. In addition to the use of multi-sensor remote sensing data, as well as the multi-scale analysis, the novelty of the current research relied on the installation of a sediment trap within the observing area in order to validate the remote sensing results and to attain a better understanding of the geomorphological evolution.

Briefly, the aim of the current study was to demonstrate that the evolution of the entire western coast of Lefkada Island is mainly controlled by seismicity and less by climatological or other factors. This knowledge is particularly crucial for the local decision makers who develop infrastructure on the specific coast where thousands of tourists gather every summer. Our approach combined remote sensing data, field measurements, and GIS techniques.

2. Materials and Methods

2.1. Study Area

Greece, and especially the western part, where Lefkada Island is located (Figure 1), has been characterized as the region displaying the highest seismicity within Europe [22–24]. Earthquakes occurring in this specific region are associated with the subduction of the African plate and the continental collision of the Apulian platform [25–27]. The dextral strike-slip Cephalonia Transform fault constitutes the prevalent tectonic structure in this region [28–30]. Moreover, seismicity in conjunction with the geological setting of western Lefkada are the main triggering factors for the occurrence of landslides [31]. In more detail, the bedrock of the west overhanging cliff of Lefkada consists of Mesozoic carbonate rocks with intercalation of Tithonian–Berriasian black schist layers, along with Pleistocene red-brown clays and conglomerates [32,33]. The Pleistocene period resulted in the formation of a series of fault-controlled basins located in the inland part of the west coast, while Holocene scree and debris cones are detected along the western coast of the island and on the cliffs located north of Vassiliki valley [32,33]. These screes are primarily composed of angular cobbles and rare boulders attaining a thickness of 1–10 m (Figure 2), which are

rested on the hillslopes that render the area vulnerable to mass movements [34]. Structural mapping along the west coast indicates its deformation through a dense array of, more or less, NS-trending strike-slip faults.

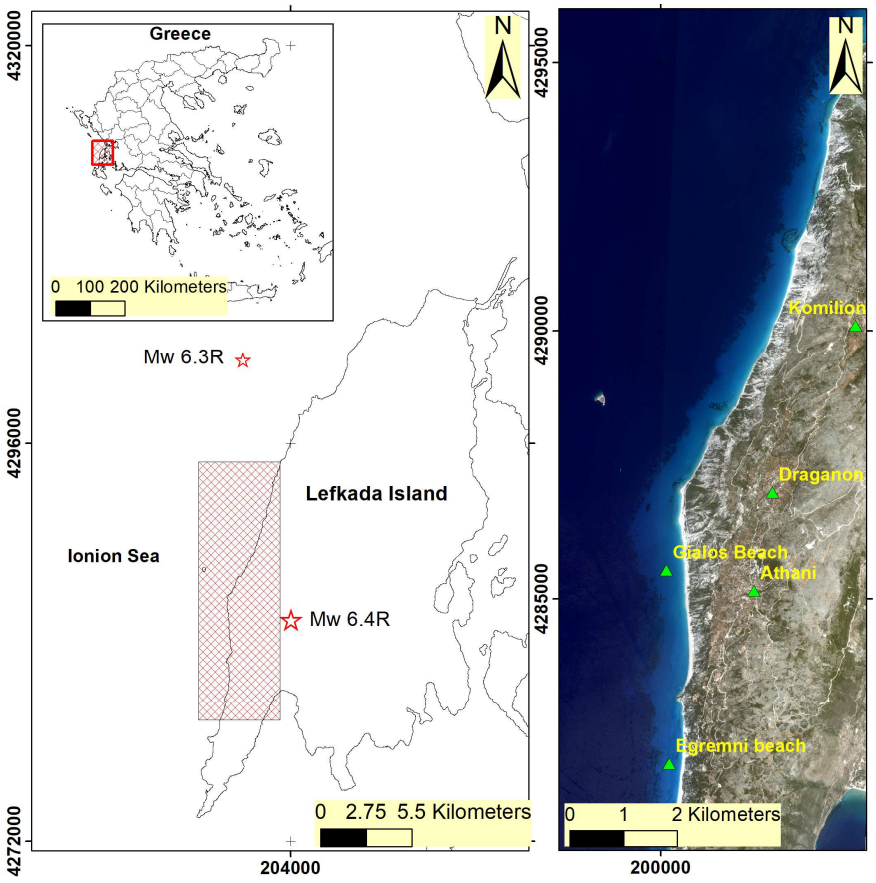

Figure 1. Location of the study area within Greece and the respective Pleiades orthophoto.

Figure 2. Outcrop of screes in the study area showing that angular mixtures of sediments are prevalent, despite the fact that there are also wide grain size distributions primarily concentrated in the sizes of the cobbles and sands. Boulders in this assemblage are rare. The width of the photo is 4 m.

A 6.2 Mw earthquake occurred on 14 August 2003 offshore in the northern part of Lefkada [35,36]. A few years later, on 17 November 2015, another strong earthquake (Mw 6.4) struck the western inland part of the island. Since then, a large body of studies has been carried out concerning the analysis of the co-seismic deformation, the slip distribution, the source parameters, and the slip model [37–42]. In addition to the seismotectonic perspective, other researchers have examined the macro-seismic effects of these events via the recording of different types of mass movements as well as the identification and assessment of ground failures [43–45]. Two characteristic images acquired from the UAV on November 2020 depicting the mass movements and rockslides on the coastal area of Egremni are presented in Figure 3 [19,20]. Extending from this, respective studies focused on using statistical analysis models, simulations, or fuzzy logic to create susceptibility maps in order to obtain useful information about the spatial distribution of potential earthquake-induced mass movements [46–48].

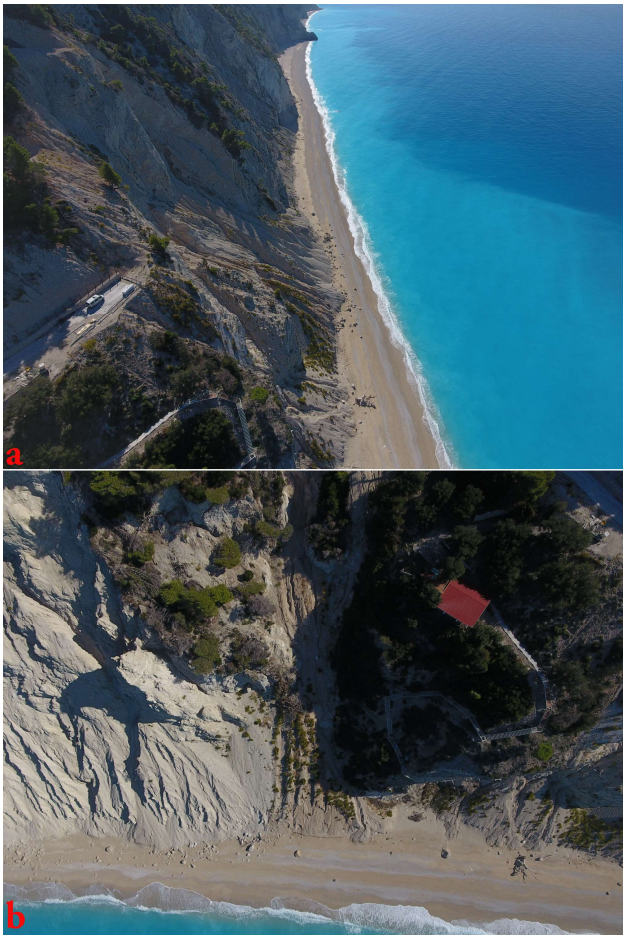

Figure 3. (**a**) Panoramic view of Egremni coastal area from the north to the south. Mass-wasting materials and rocks detached from the cliff are laying on the beach. (**b**) A close-up photo of the coast facing to the east. Several rocks detached from the upper cliff are accumulated on the coast.

2.2. Materials

2.2.1. Remote Sensing Data

In the present work, the western cliffs of Lefkada Island were investigated using remote sensing techniques. In fact, the utilization of such data was considered imperative as the study area covers a 20 km-elongated part of the island. Multi-sensor data were selected due to the fact that very high-resolution data are not freely available nor can they be acquired on a regular basis, such as medium resolution imagery (Landsat and Sentinel-2 MSI).

In this framework, our dataset was consisted of: (a) medium resolution imagery acquired from Landsat satellites and (b) high-resolution data, such as analogue aerial photographs on a 1:10,000 scale acquired by the Hellenic Military Geographical Service (HMGS), digital orthomosaics of the years 2008 and 2016 obtained from the National Greek Cadastre and Mapping Agency, as well as IKONOS and Pleiades satellite imagery (Table 1). In the following paragraph, more details have been provided regarding the processing of these different datasets. Specifically, Landsat images obtained from June to August of the years 2003, 2004, 2015, and 2016 were imported and processed onto Google Earth Engine (GEE). This specific acquisition period was selected due to the lower cloud coverage. Regarding the high-resolution data, the older set of data used was an IKONOS bundle image acquired in 2000; the spatial resolution was 1 m and the image was processed in Leica Photogrammetry Suite. The next dataset, dating back to 2004, was composed of twenty analogue airphotos obtained from the HMGS. The airphotos were scanned in Tagged Image File Format (TIFF) in 1200 dots per inch (DPI) without compression and afterwards they were orthorectified using a suitable bloc file created in LPS. To orthorectify the IKONOS imagery and the airphotos, an orthomosaic and a digital surface model (DSM) of the Greek cadastral were utilized. These specific products, dated back to 2008, are available upon request and they constitute the more accurate official dataset for the Greek territory. In addition, an orthorectified Pleiades bundle imagery was purchased from Airbus. The spatial resolution of the data was 0.5 m and the acquisition date was 13 June 2015, i.e., five months before the earthquake. Finally, a Pleiades stereo pair was obtained from the Enceladus Hellenic supersite. The stereo pair was acquired on 13 October 2016, i.e., a few months after the earthquake. There are both panchromatic and multispectral data with 0.5 and 2 m spatial resolution. The specific imagery covers the whole island and it was also processed in LPS using ground control points from the precise cadastral products and the fieldworks. Ground control points were measured using a Leica GS08 Real Time Kinematic sensor. The processing of the Pleiades stereo pair produced an orthophoto with a spatial resolution of 0.5 m and a DSM with a 1.5 m spatial resolution. This specific DSM was down-sampled in order to be comparable with the respective one from the Greek cadastral. The remote sensing data, as well as their sources and spatial resolution, are described in Table 1. More details about data processing via LPS are given in previous studies [20,49].

Table 1. Remote sensing data used in the current research.

Year	Data	Source	Number of Photos	Spatial Resolution	Type
2000	IKONOS bundle imagery	USGS	1	1.00 m	Digital
2004	Airphotos		20	1.00 m	Analogue
2008	Orthomosaic		1	0.50 m	Digital
2008	DSM			5.00 m	Digital
2015	Pleiades bundle		1	0.50 m	Digital
2016	Pleiades stereo pair		1	0.50 m	Digital
2003	Landsat-5		Multiple	30.00 m	Digital
2004	Landsat-5		Multiple	30.00 m	Digital
2015	Landsat-8		Multiple	30.00 m	Digital
2016	Landsat-8		Multiple	30.00 m	Digital

2.2.2. Field Data

Dry ravel is the process of the rolling, bouncing, and sliding of loose material down a slope, which is the dominant transformational process along the cliffs of the west parts of Lefkada Island [50]. A sediment trap was used for the first time on Lefkada Island to collect sediment flux through dry ravel (Figure 4). The installation site is located on Egremni cliff, within the tectonically active zone of the CTF. The climate in this specific region is semiarid Mediterranean, and its lithology consists of moderate to weakly consolidated Pliocene–Pleistocene fanglomerate, resulting in a soil-mantled hillslope. The sediment trap was constructed from a roof gutter, which was one meter long and 0.25 m in height.

Removable covers were placed at the ends of the trap in order to collect sediment as well as to clean the trap. To collect sediments, we used a brush and a plastic bag that was mounted at one of the ends of the gutter. This selected type of trap imitates a similar experiment by Gabet [51] since most of the sediment flux in the area is coarse grained. The installation of the trap was performed three years after the 2015 earthquake that mobilized a wide sliding zone [20]. The total duration of this experiment was almost two years, ranging from November 2018 to October 2020, when the last sample was collected. Afterwards, the trap was destroyed for an unknown reason.

Figure 4. The sediment trap that was placed on the overhanging cliff located in Egremni beach.

It is worth mentioning that dry ravels are complicated phenomena that involve mixtures of sediments with wide grain size distributions. In light of this, we assumed that we would lose the finer fractions of the granular phase, e.g., clay and silt, as they mix with water, due to the fact that our sediment trap was not able to collect water. The coarser grain clast of angular cobble captured in the sediment trap was at the maximum diameter of 135 mm (Figure 5). The possible grain size of the larger cobbles or even boulders not captured in the trap are rare [20]. Therefore, we considered the sediment in the trap as representative of the dry ravel process in the area. Larger boulders can be detected and mapped using high resolution imagery acquired with UAVs [20,21]. Concerning the rest

of the sample, we applied dry sieving with a mechanical shaker. The used sieves were wire-meshed and stacked, with mesh sizes spaced primarily at 1 ϕ intervals. The samples were dried for 24 h and they were weighed before sieving. The mass and the respective collection periods of each of the samples are presented in Table 2. Six sieves with the following diameters: 8 mm, 5.6 mm, 4 mm, 2 mm, 0.50 mm, and 0.25 mm were used to separate the collected material into different classes, i.e., gravels (8 mm) to fine sand (0.25 mm).

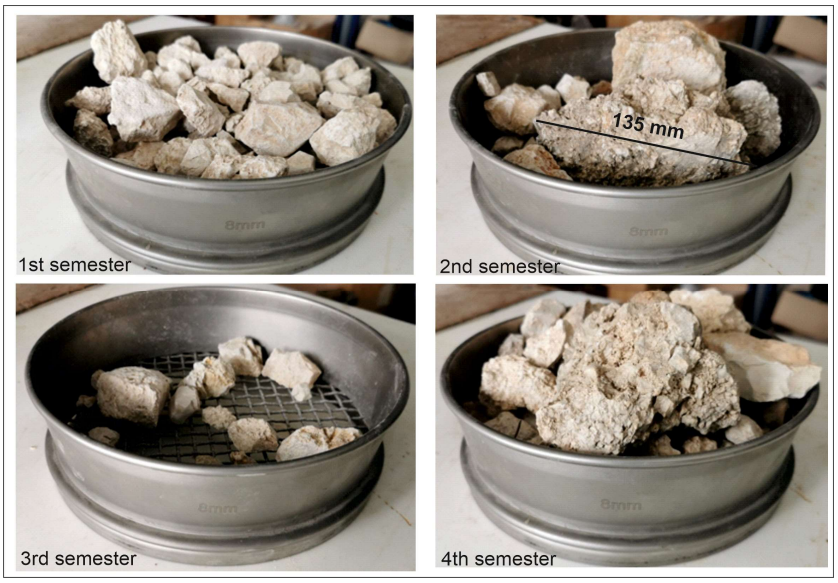

Figure 5. Photos during sieving showing the maximum clast collected from the trap during the four sampling semesters.

Table 2. Sampling periods and sediment weight of the sedimentary trap in the Egremni site.

Sampling Periods	Sediment Weight	Precipitation (mm)	Earthquakes in R	Earthquake Energy Release (Joules)
3 November 2018–30 April 2019 1st semester	3206 g/or 534 g/month	856.50	3.4, 3.7, 3.5, 4.1, 3	10.63×10^{-10}
30 April 2019–9 November 2019 2nd semester	1393 g/or 232 g/month	263.9	3.4	1.36×10^{-10}
9 November 2019–17 March 2020 3rd semester	1202 g/or 240.4 g/month	712.50	3.1, 3.5	2.4×10^{-10}
17 March 2020–3 October 2020 4th semester	2790 g/or 429.2 g/month	468.8	3.6, 3.2, 3, 4.1	7.47×10^{-10}

2.3. Methodology

In order to effectively assess the evolution of the western coastal zone of Lefkada Island, as well as to examine the influence of seismicity on the slope instabilities, we applied a complementary approach based on multi-sensor remote sensing data and in situ field observations (Figure 6). Specifically, medium resolution imagery acquired from the Landsat satellites was utilized to detect the areas displaying large alterations in vegetation before and after the last two strong earthquakes. In this framework, we computed the normalized difference vegetation index (NDVI) using Landsat imagery in the GEE platform. The

NDVI represents the photosynthetic activity occurring in a pixel and is calculated using Equation (1):

$$\mathrm{NDVI} = \frac{(\mathrm{NIR} - \mathrm{Red})}{(\mathrm{NIR} + \mathrm{Red})}. \quad (1)$$

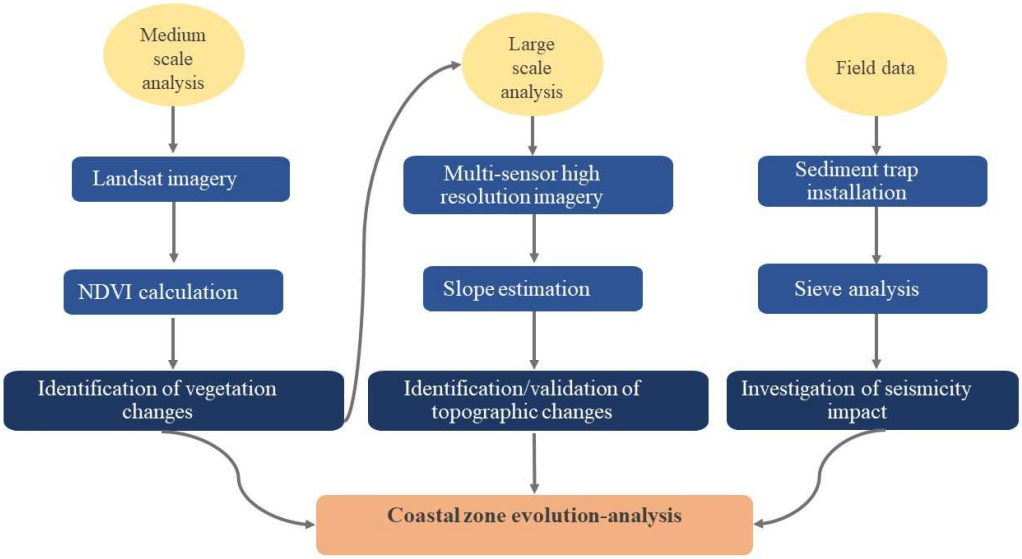

Figure 6. Diagram illustrating the applied methodology.

The index ranges between −1 and 1, where a higher NDVI corresponds to a higher level of photosynthetic activity. Specifically, bands 3 and 4 of the Landsat 8 mission were utilized to compute NDVI indices before and after the 2015 earthquake. Afterwards, these NDVI indices were imported into a GIS environment, where they were subtracted to identify vegetation changes (Equation (2)):

$$\mathrm{dNDVI} = \mathrm{NDVI}_{\mathrm{before}} - \mathrm{NDVI}_{\mathrm{after}}. \quad (2)$$

Areas which displayed large vegetation changes were further investigated using multi-sensor high-resolution data. To validate these vegetation differences, we used Pleiades multispectral data. In particular, a band combination (4, 3, and 2), corresponding to the near infrared, red, and green parts of the spectrum, was applied to highlight the vegetation canopy. Moreover, to identify topographic changes, we performed slope calculation and statical interpretation over these areas utilizing high-precision DSMs (Table 1).

At the same time, a sediment trap was placed within the area of interest in order to define the influence of seismicity and precipitation on slope integrity during the inter-seismic era. The collected samples were analyzed via the sieving technique.

More details concerning the applied methodology are provided in the following section.

3. Results

3.1. Google Earth Engine

To identify vegetation modifications before and after the 2015 earthquake, we computed NDVIs using Landsat imagery in the GEE platform. In particular, NDVI indices for the years 2015 and 2016 over the study area were estimated using Landsat images obtained from June to August. Figure 7 depicts the result of such procedure. Of note, Figure 7a displays the NDVI of 2015, while Figure 7b corresponds to the NDVI after the 2015 earthquake, respectively. As can be observed, extended vegetation modifications were detected along the entire coastal region. To isolate theses alterations from the stable vegetation, we calculated the difference between the NDVI of 2015 and the respective one

of 2016. Figure 7c displays the difference between these two indices. The red color marks the areas with the greatest vegetation changes.

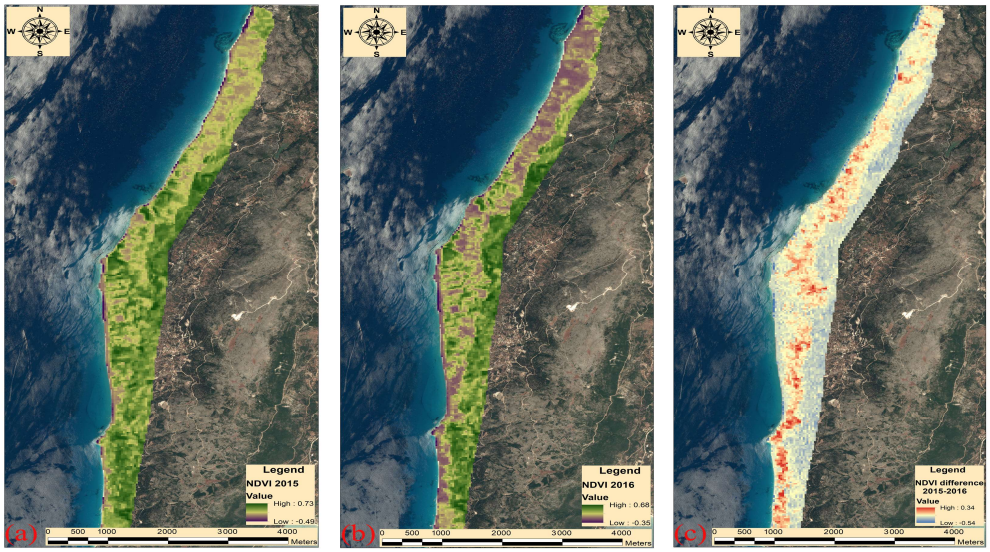

Figure 7. NDVI results before (**a**) and after (**b**) the 2015 earthquake, as derived from the processing of Landsat imagery in the GEE. (**c**) NDVI difference between the years 2015 and 2016, as derived from the processing of Landsat imagery in the GEE.

3.2. High-Resolution Remote Sensing Data

As described in the previous section, high-resolution remote sensing data has been used to identify topographic changes along the western cliff of Lefkada Island. The processing of the data has been divided into two parts, i.e., (a) optical recognition of the changes and (b) interpretation of the results through statistical analysis.

3.2.1. Change Detection

Specifically, we compared the orthophotos acquired by Pleiades before and after the November 2015 earthquake over four areas along the western coastline of Lefkada. At the same time, we also analyzed two DSMs. The first was dated back to 2008 and was obtained from the Greek cadastral, while the second was generated from Pleiades stereo pairs that were acquired in 2016. According to the cadastral official specifications, the DSM had a vertical accuracy ranging between 2 and 3 m. The respective accuracy of the Pleiades DSM was found to be considerably better than 1.5 m.

The analysis of the aforementioned revealed that the 2015 earthquake provoked severe changes to the cliffs along the coastline. In further detail, Figure 8 depicts the coastal area of Egremni as derived from Pleiades orthophoto before and after the earthquake. It is obvious that the cliff has totally changed; the inclination was increased (Figure 9) and there is a serious loss to the vegetation cover of the area (Figure 8). As can be observed in Figure 8, the road leading to the beach was totally destroyed. In the specific part of the coast, the length of the landslide was measured at 135 m. In the middle of the beach, there was a big rock outcrop lying next to the sea, while, on both sides of the rock, the cliff has impressively changed. In 2016, the cliff moved backwards, and the beach was covered through debris flow. The landslide length was found to have overpassed 185 m at the that point. Added to this, areas with a slope inclination greater than 45 degrees were increased along with the absolute value of the highest inclination (i.e., 84.6 degrees instead of 82.5 degrees in 2015). Generally speaking, all areas along the beach next to the sea presented higher inclination values in 2016 as a result of mass-wasting processes. The areas with the greatest vegetation losses, related to the 2015 earthquake, have been presented with red shades in Figure 10. NDVI indices for the years 2015 and 2016 have been calculated based on Pleiades multispectral data with a spatial resolution of 0.5 m. These

results verified the NDVI changes captured by the medium resolution data in the GEE. Red shades correspond to NDVI differences between 2015 and 2016, while the black dashed line indicates the landslide extent. A very high vegetation difference (loss) resulted from the 2015 earthquake was identified along the Egremni cliff. The width of the beach displaying the largest changes (change of inclination, vegetation loss, and mass movements) was measured to be about 1.5 km.

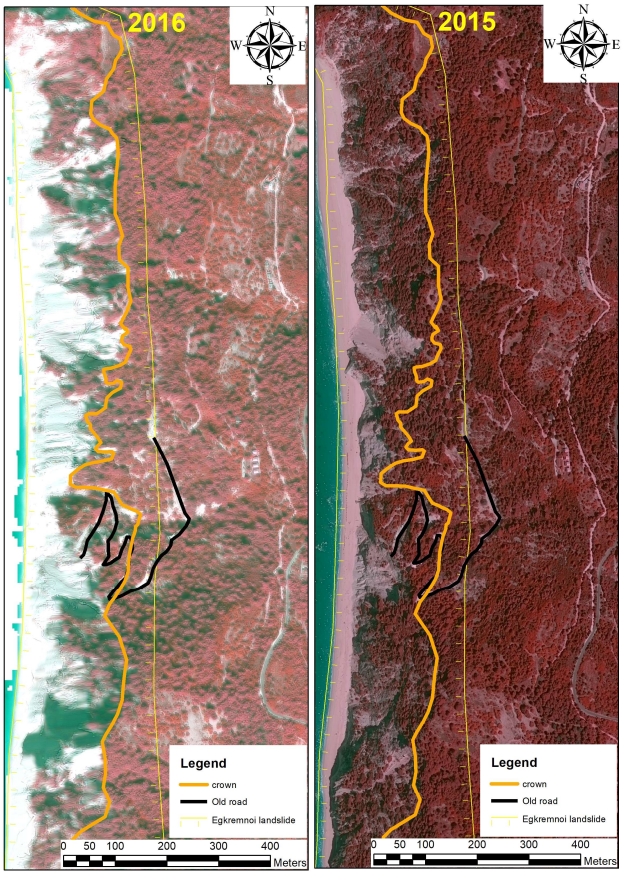

Figure 8. On the (**left**), a Pleiades orthophoto of the Egremni coast in 2016 is presented. On the (**right**), the same area has been displayed in the Pleiades orthophoto in the year 2015. The yellow line indicates the landslide extent. The backwards movement of the cliff is evident on the left image. The orange line indicates the landslide crown while the black line represents the old road to the beach that was destroyed.

The detected changes along the Okeanos cliff are presented in Figures 11 and 12. On the left of these figures, the Pleiades orthophoto of the Okeanos coast in 2016 is presented in both figures, while the right side depicts the same area in 2015. The yellow line indicates the landslide extent. The backwards movement of the cliff was evident on the left image. In fact, the pre-existing landslides were deemed to have been reactivated and enlarged both in their lengths and widths. The most characteristic example of such phenomenon is presented in Figure 12, which presents an enlarged part of Figure 11. As can be seen, the crown of the landslide reached the buildings on the top of the hill in 2016 (upper part of Figure 12), while the total length of the landslide body exceeded 237 m (upper part of Figure 12). Slope maps of the Okeanos coast before and after the occurrence of the 2015 earthquake are displayed in Figure 13. Large changes to the inclination were detected, especially at the south part of the coast. The lower inclination values (green shades) were replaced by red shades nearer to the sea, indicating that a large body of debris flow has moved from the cliff to the beach, altering the relief. Furthermore, the areas with a slope inclination of higher than 45 degrees (red color) were expanded in 2016, and the absolute

value of the highest inclination increased 5 degrees after the earthquake (78.6 degrees in 2016 instead of 73.6 in 2015, respectively).

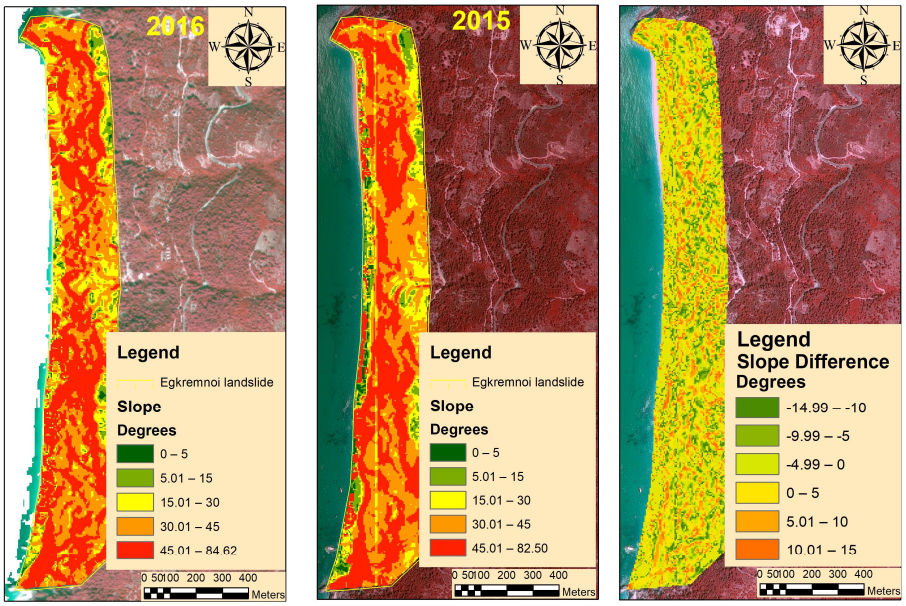

Figure 9. On the (**left**), the slope map of the Egremni coast in 2016 is displayed. In the (**middle**), the same area is displayed in the year 2015. Color changes indicate the changes to the cliff inclination before and after the 2015 earthquake. The slope difference values are presented in the (**right**) image.

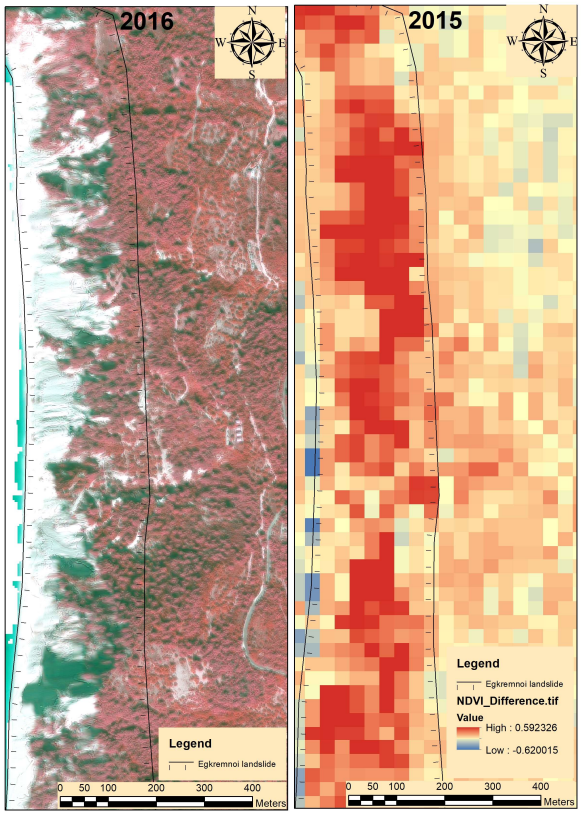

Figure 10. On the (**left**), a Pleiades orthophoto of the Egremni coast in 2016 is presented. On the (**right**), the NDVI difference between the years 2015 and 2016 is displayed. The black dotted line indicates the landslide extent. It is obvious that there is a great loss of vegetation as a result of the earthquake that occurred in 2015.

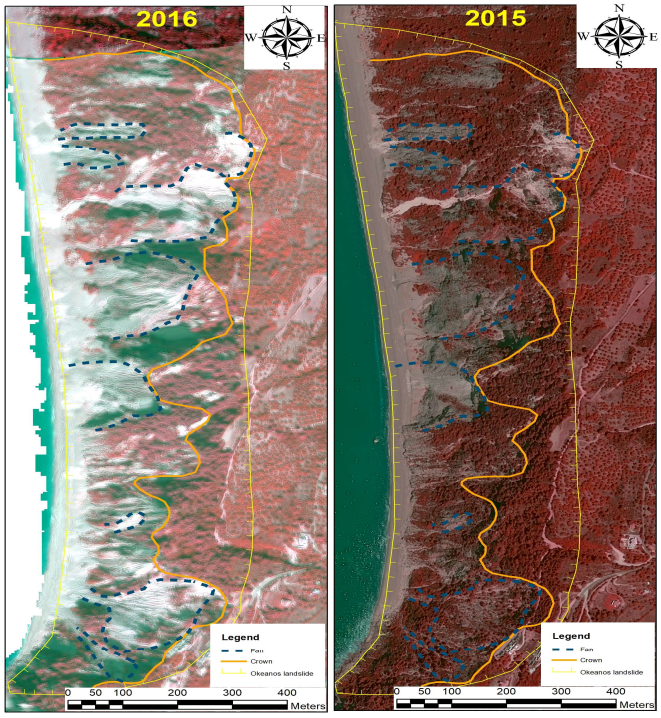

Figure 11. On the (**left**), a Pleiades orthophoto of the Okeanos coast in 2016 is presented. On the (**right**), the same area is displayed in the year 2015, as captured by the Pleiades orthophoto. The yellow line indicates the landslide extent. The backwards movement of the cliff is evident on the left image.

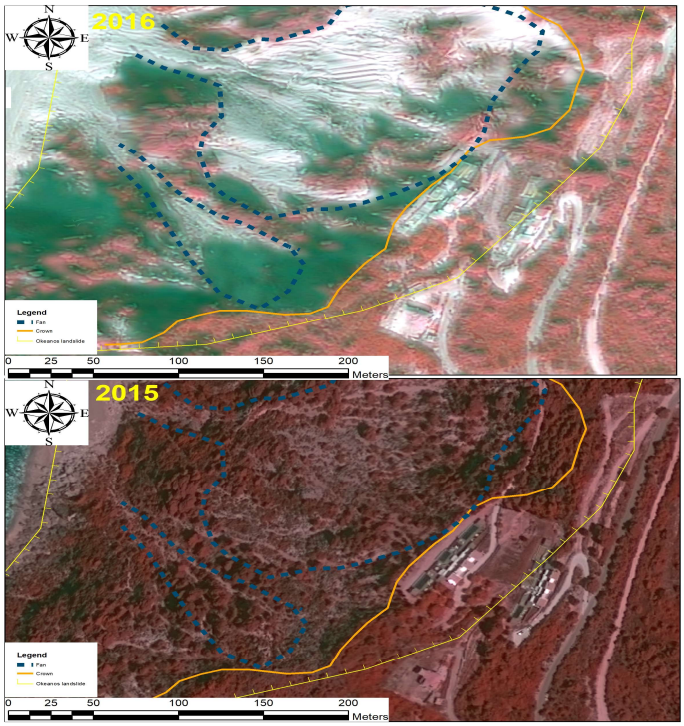

Figure 12. Enlargement of the previous figure. On the (**top**), a Pleiades orthophoto of the Okeanos southern coast in the year 2016 is displayed. On the (**bottom**), the same area has been captured with the Pleiades orthophoto in the year 2015. The backwards movement of the cliff is evident on the upper image. The landslide affected the buildings presented on the right part of the area. The orange line indicates the crown of the landslide.

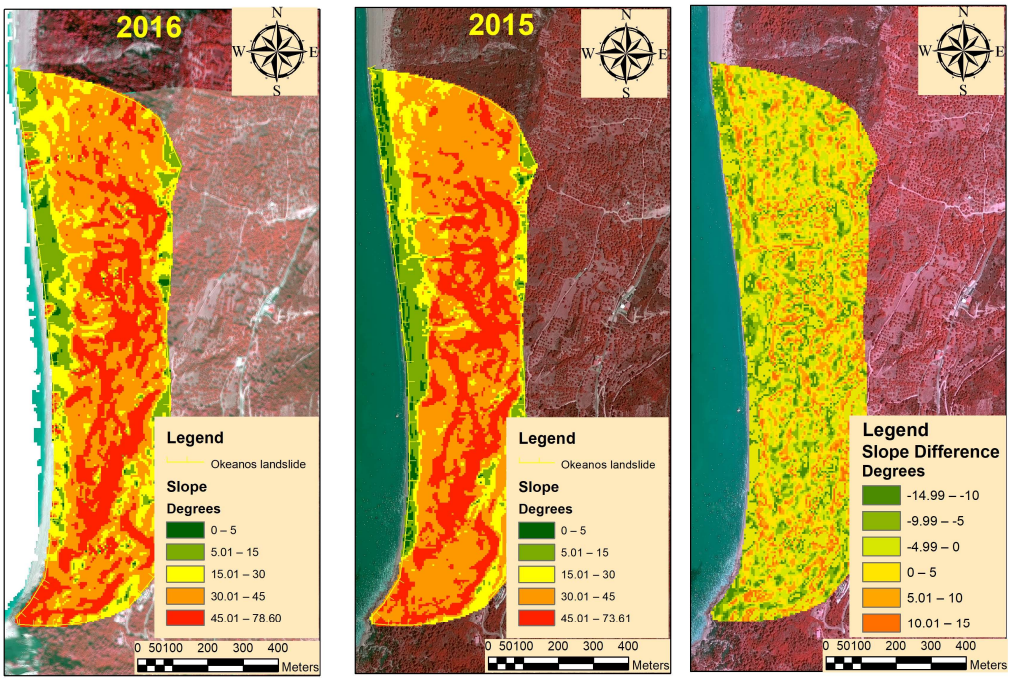

Figure 13. On the (**left**), the slope map of the Okeanos coast in 2016 is displayed, while in the (**middle**), there is the respective map of the year 2015. Color changes indicate the changes to the cliff inclination before and after the earthquake occurrence. The slope difference values are presented on the (**right**) image.

Similar topographic changes arising from the 2015 seismicity were mapped in the Gialos coast as presented in Figures 14 and 15. A Pleiades orthophoto of the Gialos coast in 2016 is presented in the left part of Figure 14. The same area in 2015 is displayed in the right part of Figure 14. The yellow line indicates the landslide extent. The detected landslides in the specific part have been grown in length and width, while the backwards movement of the cliff is evident on the left image (Figure 14). The loss of vegetation in the south part of the coast reveals the mass-wasting processes moving the material from the upper cliff to the lower areas close to the sea. The total extent of the affected area overpassed 2.7 km in width and 0.9 km in length. The slope maps of the Gialos coast before and after the occurrence of the 2015 earthquake are presented in Figure 15. Large inclination changes were identified in the southern part of the coast. Areas with a slope inclination higher than 45 degrees (red color) have been increased in 2016 and the absolute value of the highest inclination has been altered by almost 11 degrees after the earthquake (78.6 degrees in 2016 instead of 67.9 in 2015, respectively). At the same time, areas with slopes ranging from 5–15 degrees have surged, which indicates that the debris material has been moved from the upper part of the cliff to the lower.

Finally, Komilio coast, which is located in the northern part of the analyzed western cliffs, was also affected by the 2015 seismicity. Figures 16 and 17 depict the changes to the cliff's morphology and slope. Specifically, a Pleiades orthophoto of the Komilio coast in 2016 is presented in the left part of Figure 16, while on the right, the same area mapped in the year 2015 is displayed. The yellow line indicates the landslide extent and the black line depicts the dirty road network driving to the beach. The debris material covered the middle part of the coast as well as a segment of the road (black line). The width of this material was 200 m while its length was almost 400 m (Figure 16). The whole landslide extent (i.e., from the beach to the crown) at this specific site overpassed 550 m. Meanwhile, areas with intermediate slope values (orange color) have been increased, while the areas marked with the red color (higher inclination) have been diminished (Figure 17).

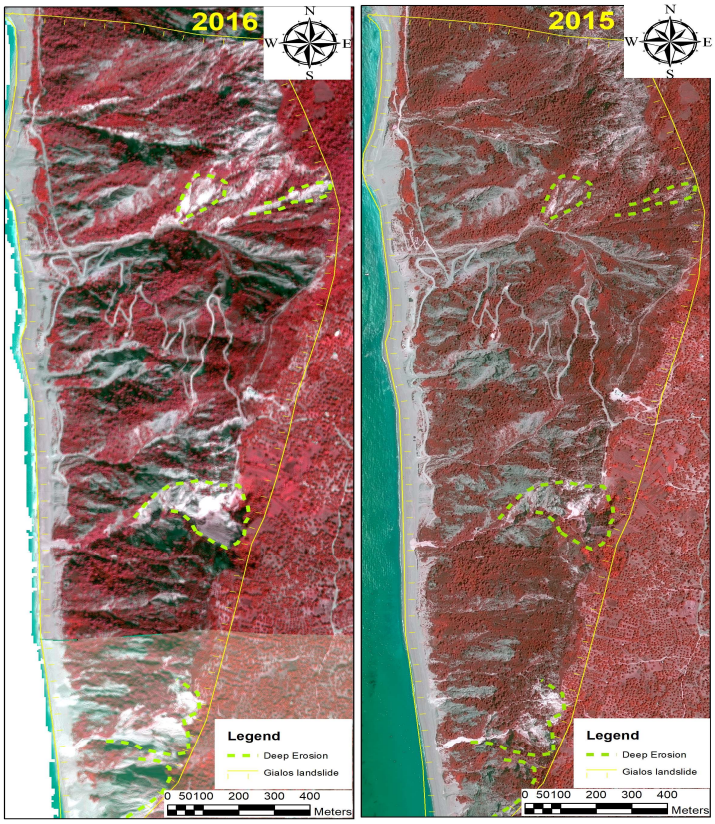

Figure 14. On the (**left**), a Pleiades orthophoto of the Gialos coast in 2016 is displayed. On the (**right**), the same area has been presented in a 2015 Pleiades orthophoto. The yellow line indicates the landslide extent. The backwards movement of the cliff is evident on the left image. The green dashed line indicates areas with deep erosion.

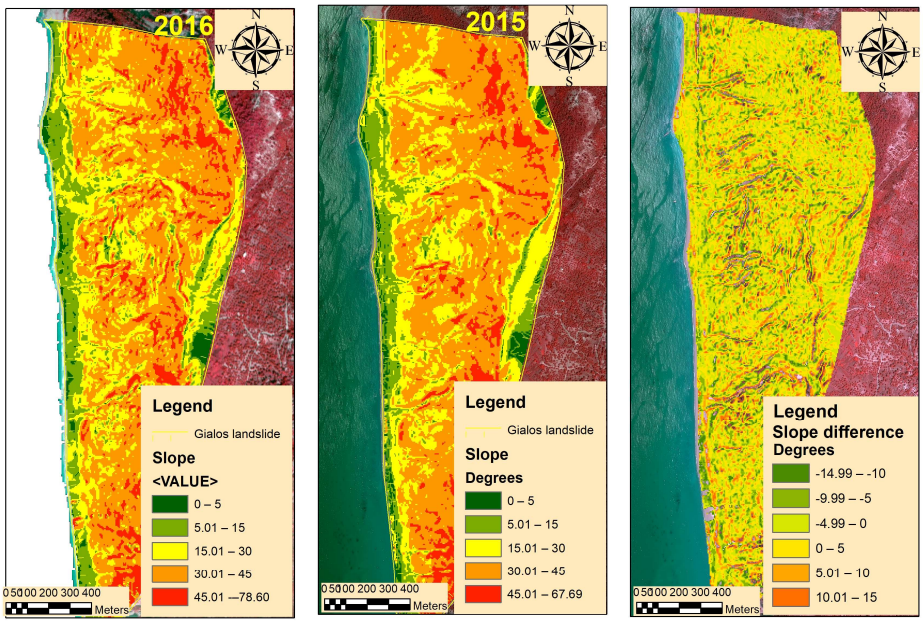

Figure 15. On the (**left**), the slope map of the Gialos coast in 2016 is displayed. In the (**middle**), the same area is displayed in the year 2015. Color changes indicate the changes to the cliff inclination before and after the 2015 earthquake. On the (**right**) image, the slope difference values are presented.

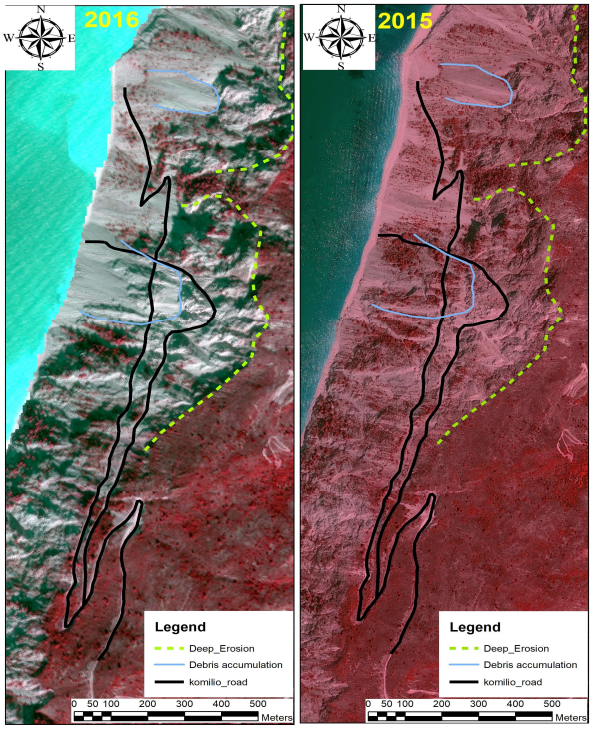

Figure 16. On the (**left**), a Pleiades orthophoto of the Komilio coast in 2016 is displayed. On the (**right**), the same area has been presented in a 2015 Pleiades orthophoto. The backwards movement of the cliff is evident on the left image. The green dashed line indicates areas with deep erosion, while the blue line shows areas with debris accumulation.

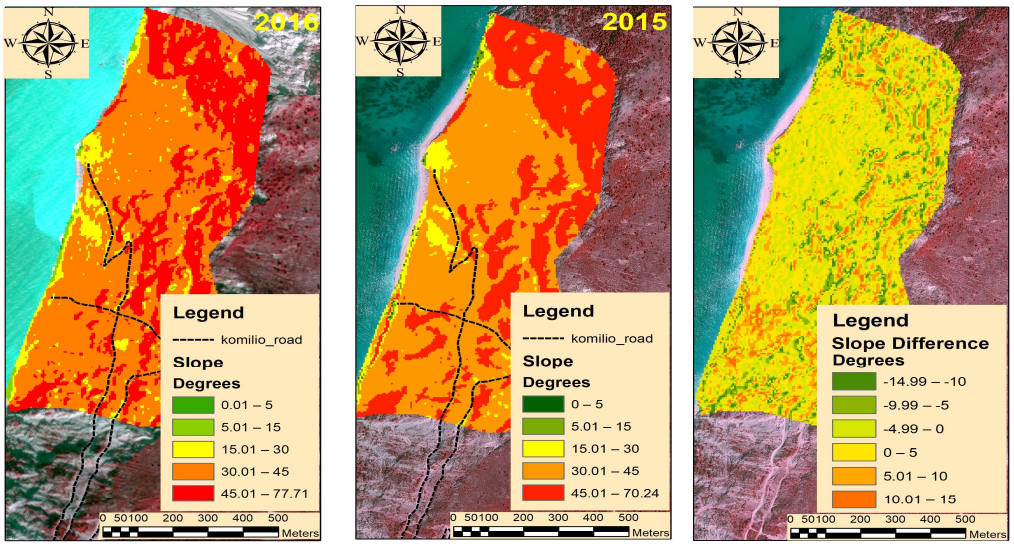

Figure 17. On the (**left**), the slope map of the Komilio coast in 2016 is displayed. In the (**middle**), the same area has been presented in the year 2015. Color changes indicate the changes to the cliff inclination before and after the 2015 earthquake. On the (**right**) image, the slope difference values are presented.

3.2.2. Numerical Evaluation of the Changes

The analysis of these slopes before and after the 2015 earthquake confirmed the results derived from the processing of medium and high-resolution remote sensing imagery. The statistics of the five slope classes (i.e., 0–5, 5.01–15, 15.01–30, 30.01–45, and higher than 45.01 degrees) were calculated and the diagrams for the areas of Egremni, Okeanos, Gialos, and Komilio are presented in Figures 18–21, respectively. Generally, an increase in the

inclination values ranging from 15 to 30 degrees was observed in all the study areas. At the same time, an increase at higher class slope values (above 45 degrees) was detected, which was determined to be associated with the occurrence of mass movements after the 2015 earthquake, modifying the relief in a steeper manner. Meanwhile, a decrease in the areas with slope values ranging from 30 to 45 degrees was detected in the Egremni, Gialos, and Okeanos coastal areas, resulting in the steeper transformation of the relief along the subsequent accumulation of the debris flow in areas with lower inclination values (15–30 degrees). Komilio coast is an exception to the aforementioned procedure. In particular, these specific areas were also affected by the 2003 earthquake, meaning therefore that less debris material was prone to the sliding phenomena. In fact, slope analysis confirmed this observation since minor slope changes between 2015 and 2016 were detected.

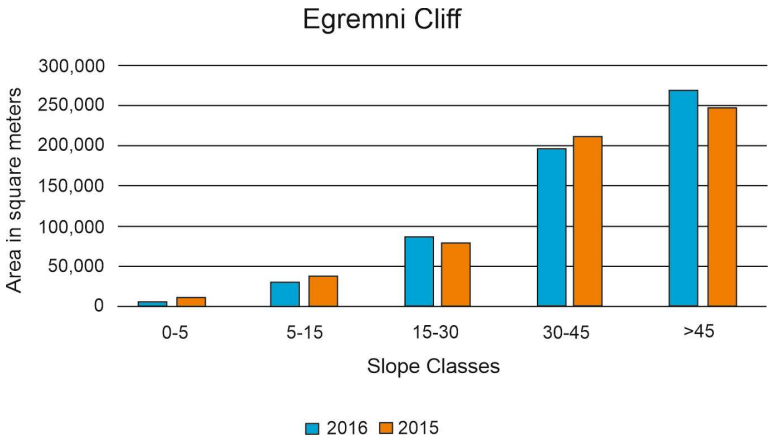

Figure 18. Analysis of the slope classes between 2015 and 2016 for the Egremni cliff.

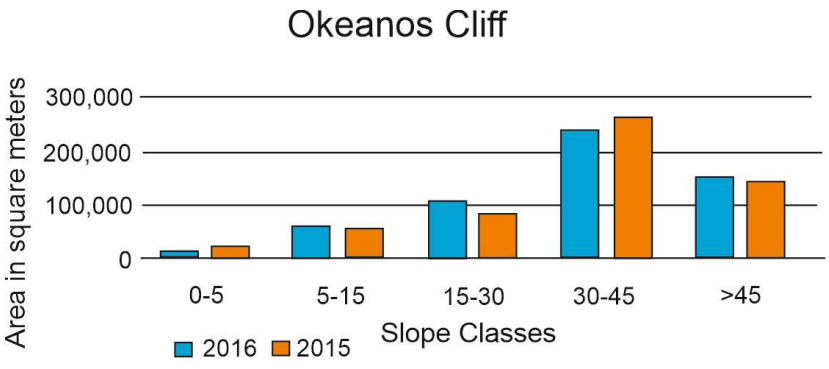

Figure 19. Analysis of the slope classes between 2015 and 2016 for the Okeanos cliff.

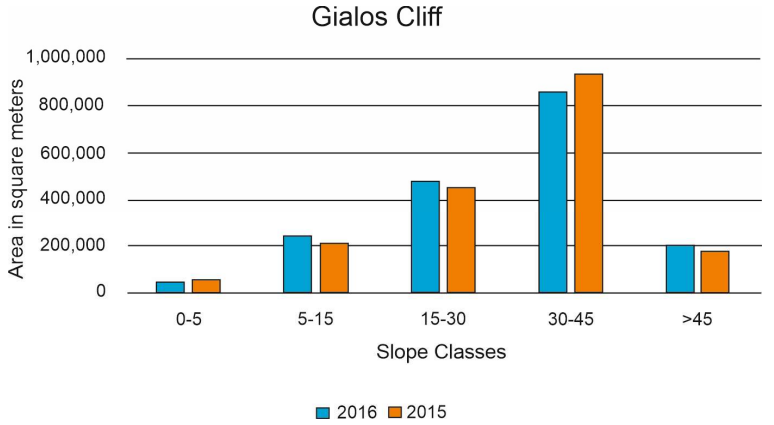

Figure 20. Analysis of the slope classes between 2015 and 2016 for the Gialos cliff.

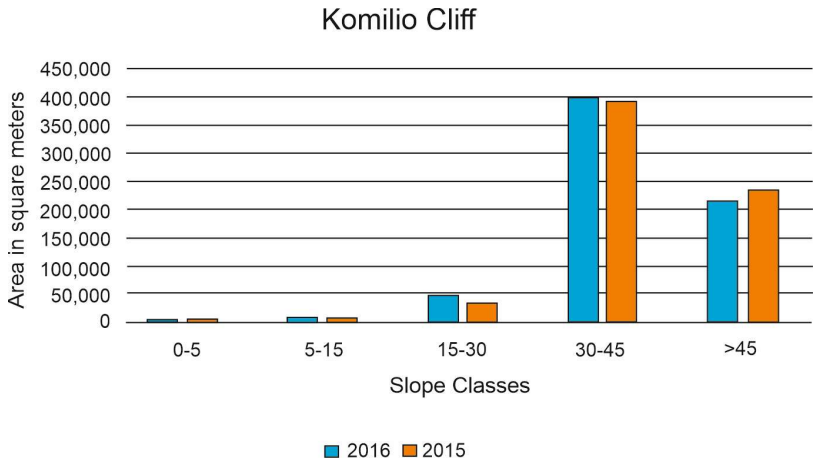

Figure 21. Analysis of the slope classes between 2015 and 2016 for the Komilio cliff.

3.3. Field Data

The analysis of these collected samples pointed out that sediment productivity during the four semesters of the ravel activity was bimodal and varied from a mean of 236.28 to 481.76 gr/month (Table 2). The lower sediment productivity, which was almost half of the highest, was recorded during the second and the third semesters (Table 2). The productivity of these two intervals seemed to not be associated with the observed precipitation. Since the sediment productivity from 9 November 2019 to 17 March 2020 was approximately one third of the productivity during the period 3 November 2018–30 April 2019, we can consider fairly that the controlling factor underlying the sediment productivity is the seismicity. Indeed, the seismicity during the periods of increased sediment productivity was quantitatively denser and stronger throughout the first and the fourth semesters of the experiment operation (Table 2).

In terms of the sieving analysis, the first and fourth semesters' samples indicated the existence of all classes of sediments i.e., medium gravels and clasts larger than 8 mm in diameter, fine and very fine gravels, and coarse, medium, and fine sand (Table 3). Figure 22 depicts the angular and subangular gravels with a diameter > 8 mm and the coarse sand of the first semester sample during the sieving analysis. On the contrary, sedimentary samples of the second and third semesters mainly consisted of medium and coarse gravel sediments, while all the other sediment classes were relatively absent (Table 3). Hence, it is evident that the existence or absence of seismicity in this area constitutes a significant triggering factor associated with different sediment classes. Specifically, seismicity appears to trigger all possible classes of sediments ranging from very fine sands to coarser then medium gravels.

Table 3. Classification of the four semester samples as collected from the sediment trap.

Classification	First Semester [1]	Second Semester [1]	Third Semester [1]	Fourth Semester [1]
Medium gravel (8 mm+)	2058	1387	1081	2232
Fine gravel	230	0	17	110
Very fine gravel	182	0	13	84
Coarse sand	270	2.3	22	131
Medium Sand	372	2.4	53	185
Fine sand	83	1.3	16	48
Total weight	3206	1393	1202	2790

[1] Sediment weight in g.

Figure 22. Sieves showing angular and subangular gravels with a diameter > 8 mm and the coarse sand of the first semester sample.

4. Discussion

Both optical and radar data with medium or high spatial resolution have been used in the past for the semi or fully automatic detection of earthquake-triggered landslides [16,52–54]. Our methodology and results are in accordance with many previous studies, as summarized in the following paragraphs. One of the first attempts to implement an automated method for detecting and mapping earthquake-triggered landslides was presented in 2010 using Landsat TM and ASTER data [52]. This method was based on the vegetation mass change and used the NDVI. The usefulness of the slope change for slide recognition was demonstrated in another study [55]. In a similar study [56], the authors proposed a change detection methodology based on optical data to investigate the pre-event era and SAR data for the after event period. The NDVI was used as the first selection landslide site selection criterion while the slope was used as a verification criterion. The suitability of UAVs in the identification of landslides triggered by the 2016 Kumamoto earthquake in Japan was presented [15]. These authors managed to detect 54 co-seismic landslides ranging from very small (nine m^3) to very extended (more than 3994.6 m^3). They also mentioned the usefulness of UAVs in such studies as the specific equipment provides both orthophotos and DSMs, in addition to other advantages, such as very high resolutions, repeatability, and mobility. Aimati et al. [12] used PALSAR-2 images for detecting earthquake-induced landslides after a strong earthquake (Mw 6.6) on 2018 at Hokkaido. In accordance with our study, they used slope data to ensure that the detected relief changes were indeed due to landslides. Added to this, Landsat images before and after the seismic event and a 20 m DEM were processed in order to detect earthquake-triggered landslides in Taiwan [57]. In another study, diverse remote sensing data, with UAV images, GF-6, and Landsat-8 imagery, with pixel sizes ranging from 0.2 m to 15 m, were selected to detect earthquake-induced landslides and the results were verified with in situ data [54]. It was found that as the spatial resolution ameliorates, the detection accuracy increased relatively as a result.

The outcomes of the current work are in accordance with the results from previous similar studies. In a study dated from 2002 [58], the coastal cliff retreat along central California was examined. It was proved that the cliff retreat was episodic, occurring in response to single large storms or seismic events. Similar to the current study, diachronic remote sensing data before and after the occurrence of storms or earthquakes were used.

In addition, to measure co-seismic vertical ground displacements in Mexico caused by the 2010 El Mayor-Cucapah earthquake, other researchers [59] followed a methodology similar to ours. A pre-earthquake LIDAR DEM was compared with a post-earthquake DEM derived from Pleiades tri-stereo imagery.

Moreover, to evaluate the historic coastal cliff retreat in the area of Conway Flat (New Zealand), orthoimages with diverse spatial resolution covering the period from 1950 to 2022 were utilized [60]. It was proved that earthquakes increased the background cliff retreat rate at this specific area by approximately 45%. Furthermore, this specific area experienced widespread cliff retreat from relatively moderate ground motion, which is quite similar to our results. As these authors mentioned, the outcomes of such studies

could serve as an important example for the calculation of long-term coastal cliff retreat over multiple earthquakes [60].

Generally speaking, it is estimated that cliffs comprise almost 80% of the coastlines on Earth [61]. In areas with high population density and high seismicity, such as California, realizing how seismicity affects the long-term retreat of coastal cliffs is a prerequisite for developing efficient forecast models [62]. According to the authors of [60], the geomorphological traces of past earthquakes could be erased, even over historical timescales, so, a holistic research should combine among others: seismic hazard analysis, geotechnical site investigations, and regional earthquake-induced landslide susceptibility analysis. Based on this point of view, the major improvement of the current study relies on the fact that we evaluated the automatically derived results from the medium resolution data (Landsat imagery on GEE) with very high-resolution imagery (Ikonos and Pleiades) and in situ measurements from the sediment trap. Another important asset of this research is that we managed to define the minimum seismic threshold that affects the integrity of the cliff.

In addition to the effects of 2015 earthquake, we also investigated the diachronic impact of the seismicity on the evolution of the western coast of Lefkada. In light of this, we have compared high-resolution satellite data (IKONOS bundle imagery) and airphotos before and after the 6.2 Mw earthquake, which occurred on 14 August 2003. As shown in Figure 23, significant topographic changes can also be detected on the Egremni cliff. Specifically, the left part of Figure 23 represents the coast of Egremni after the 2003 earthquake, while the right part corresponds to the same area in 2000. The slope has transformed in a steeper manner in the left image. The crosshair points out the same position on the cliff. The inclination of the cliff has been increased on the 2004 orthophoto. Additional photos of the coastal evolution can be found in the Supplementary Materials.

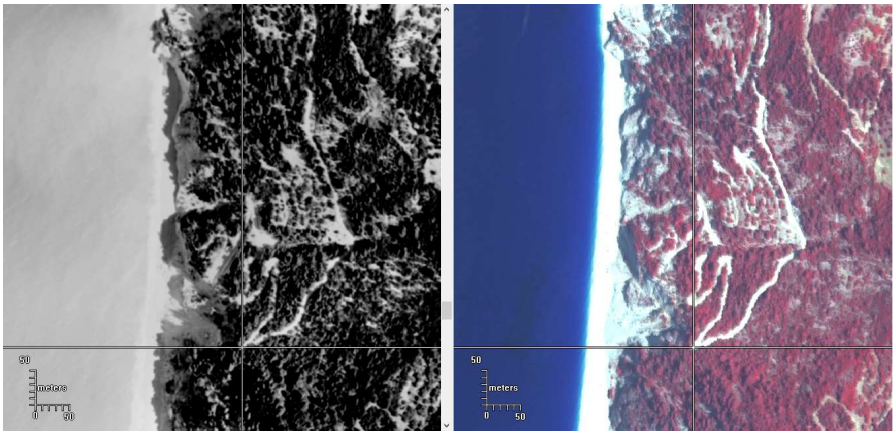

Figure 23. Relief changes on the Egremni cliff after the 2003 earthquake. On the **left** part, an orthophoto mosaic of the coast of Egremni after the 2003 earthquake is presented, while the **right** part corresponds to the same area in 2000. The slope has transformed in a steeper manner in the left image.

Summarizing the outcomes of the current study, the evolution of the western cliff of Lefkada Island is directly related to the two strong earthquakes, which occurred in the north end and close to the south, respectively. Currently, this area is affected by minor earthquakes, i.e., magnitudes < 4.1. Although these earthquake magnitudes are considered weak to trigger mass movements, they are an exception for this specific area. The analysis of the sediment trap samples proved that such magnitudes affect the west coast, which remains active in terms of the sliding phenomena. Figure 24 depicts the trap sediment concentration along the four semesters of observation in accordance with the recorded precipitation and seismicity. As can be observed, earthquakes greater than 3.0 occurred throughout the investigated era. On the contrary, 4.1 M earthquakes were recorded during the first and the fourth semesters, when the sediment concentration was

quite high. Although the highest precipitation was observed during the third semester, sediment accumulation remained low. Hence, seismicity is the main triggering factor underlying the geomorphological evolution of the cliff in this specific area.

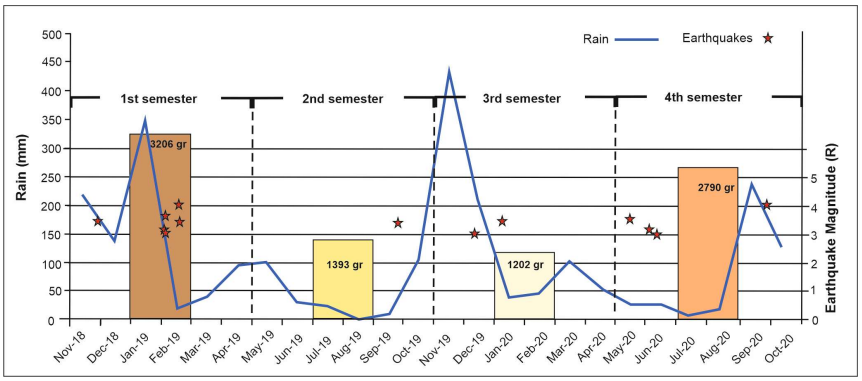

Figure 24. The trap sediment concentration along the four semesters of observation in accordance to the recorded precipitation and seismicity.

It is a commonplace that strong earthquakes trigger landslides on a national [31,63] or global level [64]. However, how low-magnitude earthquakes (i.e., M < 5.0) affect the stability of pre-existing or newly formed landslides has not been well investigated. In some recent publications, such as a study carried out in Norway, it was demonstrated that a critical magnitude of >4.5 in combination with precipitation and ground shaking can cause landslides [65]. Even smaller magnitudes, i.e., >2.5, in cases of soft sediments can provoke mass movements, as it was observed in a respective case study in Poland [66]. Regarding the national level, i.e., Greece, the threshold intensity was as low as 4.0 in the case study of the Pyrgos 1993 earthquakes [67]. These aforementioned observations are in line with the results of the current research, which attest that the 4.1 magnitude earthquakes are critical in increasing the ravel activity in the area.

To conclude, our outcomes are considerably important for the local decision makers to develop effective and safe spatial plans. Specifically, the western coasts of Lefkada are quite touristic sites during the summer period and thousands of people visit these specific beaches for swimming or other activities. Identifying that low-magnitude earthquakes (<4.1) can provoke rockfalls and/or sediments accumulation on the specific beaches is quite crucial to prevent the negative effects of natural hazards.

5. Conclusions

The current research focused on examining the impact of seismicity on the evolution of the western cliffs of Lefkada Island. In light of this, medium to very high-resolution imagery were processed, while the results were associated with in situ measurements derived from the installation of a sediment trap. The main outcomes of this study are summarized in the following:

1. The evolution of the Lefkada western coast is strongly related to seismicity.
2. Both the 2003 and 2015 earthquakes provoked inclination changes, vegetation loss, and mass movements.
3. Minor earthquakes (magnitudes < 4.1) contribute to the evolution of the cliff.
4. Since there are no wildfires or timber harvesting activities in the study area, the landform response to earthquakes is stronger than the climatic factors. Hence, heavy rain and wind are less influential in slope erosion and the cliff than the inter-seismic earthquake activity.
5. Remote sensing data and sediment trap can be combined successfully, leading to a more comprehensive understanding of the on-going processes.
6. Medium resolution GEE products and high-resolution processing results can be used as supplementary information sources.

Supplementary Materials: The following supporting information can be downloaded at: https://www.mdpi.com/article/10.3390/app13169434/s1, Figure S1: The effects of the 2003 earthquake on Komilio coast; Figure S2: The effects of the 2003 earthquake on Gialos coast.

Author Contributions: Conceptualization, K.G.N., I.K.K. and A.K.; methodology, K.G.N., I.K.K. and A.K.; software, K.G.N., A.K. and D.A.; validation, K.G.N., I.K.K. and A.K.; investigation, K.G.N., I.K.K., G.P. and A.K.; data curation, K.G.N., I.K.K., G.P. and A.K.; writing—original draft preparation, K.G.N., I.K.K., D.A. and A.K.; writing—review and editing, K.G.N., I.K.K. and A.K.; project administration, K.G.N. and I.K.K. All authors have read and agreed to the published version of the manuscript.

Funding: This research received no external funding.

Institutional Review Board Statement: Not applicable.

Informed Consent Statement: Not applicable.

Data Availability Statement: Data are available upon request due to restrictions. The data presented in this study are available upon request from the corresponding author. The data are not publicly available due to public safety reasons.

Conflicts of Interest: The authors declare no conflict of interest.

References

1. Sæmundsson, P.; Morino, C.; Helgason, J.K.; Conway, S.J.; Pétursson, H.G. The triggering factors of the Móafellshyrna debris slide in northern Iceland: Intense precipitation, earthquake activity and thawing of mountain permafrost. *Sci. Total Environ.* **2018**, *621*, 1163–1175. [CrossRef] [PubMed]
2. Huang, R.; Fan, X. The landslide story. *Nature Geosci.* **2013**, *6*, 325–326. [CrossRef]
3. Chen, J.; Che, A.; Wang, L. Cumulative damage evolution rule of rock slope based on shaking table test using VMD-HT. *Eng. Geol.* **2023**, *314*, 107003. [CrossRef]
4. Zhou, H.; Che, A.; Zhu, R. Damage Evolution of Rock Slopes Under Seismic Motions Using Shaking Table Test. *Rock Mech. Rock Eng.* **2022**, *55*, 4979–4997. [CrossRef]
5. Gischig, V.; Preisig, G.; Eberhardt, E. Numerical Investigation of Seismically Induced Rock Mass Fatigue as a Mechanism Contributing to the Progressive Failure of Deep-Seated Landslides. *Rock Mech. Rock Eng.* **2016**, *49*, 2457–2478. [CrossRef]
6. Hack, R.; Alkema, D.; Kruse, G.A.M.; Leenders, N.; Luzi, L. Influence of earthquakes on the stability of slopes. *Eng. Geol.* **2007**, *91*, 4–15. [CrossRef]
7. Meunier, P.; Hovius, N.; Haines, J.A. Topographic site effects and the location of earthquake-induced landslides. *Earth Planet Sci. Lett.* **2008**, *275*, 221–232. [CrossRef]
8. Chang, K.T.; Chiang, S.H.; Hsu, M.L. Modeling typhoon- and earthquake-induced landslides in a mountainous watershed using logistic regression. *Geomorphology* **2007**, *89*, 335–347. [CrossRef]
9. Tofani, V.; Segoni, S.; Agostini, A.; Catani, F.; Casagli, N. Technical Note: Use of remote sensing for landslide studies in Europe. *Nat. Hazards Earth Syst. Sci.* **2013**, *13*, 299–309. [CrossRef]
10. Casagli, N.; Frodella, W.; Morelli, S.; Tofani, V.; Ciampalini, A.; Intrieri, E.; Raspini, F.; Rossi, G.; Tanteri, L.; Lu, P. Spaceborne, UAV and ground-based remote sensing techniques for landslide mapping, monitoring and early warning. *Geoenviron. Disasters* **2017**, *4*, 9.
11. Liu, X.; Zhao, C.; Zhang, Q.; Peng, J.; Zhu, W.; Lu, Z. Multi-temporal loess landslide inventory mapping with C-, X- and L-band SAR datasets-a case study of Heifangtai loess landslides, China. *Remote Sens.* **2018**, *10*, 1756. [CrossRef]
12. Aimaiti, Y.; Liu, W.; Yamazaki, F.; Maruyama, Y. Earthquake-Induced Landslide Mapping for the 2018 Hokkaido Eastern Iburi Earthquake Using PALSAR-2 Data. *Remote Sens.* **2019**, *11*, 2351. [CrossRef]
13. Niethammer, U.; James, M.R.; Rothmund, S.; Travelletti, J.; Joswig, M. UAV-based remote sensing of the super-Sauze landslide: Evaluation and results. *Eng. Geol.* **2012**, *128*, 2–11. [CrossRef]
14. Peternel, T.; Kumelj, Š.; Oštir, K.; Komac, M. Monitoring the Potoška planina landslide (NW Slovenia) using UAV photogrammetry and tachymetric measurements. *Landslides* **2017**, *14*, 395–406. [CrossRef]
15. Saito, H.; Uchiyama, S.; Hayakawa, Y.S.; Obanawa, H. Landslides triggered by an earthquake and heavy rainfalls at Aso volcano, Japan, detected by UAS and SfM-MVS photogrammetry. *Prog. Earth Planet Sci.* **2018**, *5*, 15. [CrossRef]
16. Wang, X.; Fan, X.; Xu, Q.; Du, P. Change detection-based co-seismic landslide mapping through extended morphological profiles and ensemble strategy. *ISPRS J. Photogramm. Remote Sens.* **2022**, *187*, 225–239. [CrossRef]
17. Shao, X.; Ma, S.; Xu, C.; Zhang, P.; Wen, B.; Tian, Y.; Zhou, Q.; Cui, Y. Planet Image-Based Inventorying and Machine Learning-Based Susceptibility Mapping for the Landslides Triggered by the 2018 Mw6.6 Tomakomai, Japan Earthquake. *Remote Sens.* **2019**, *11*, 978. [CrossRef]
18. Pokharel, B.; Alvioli, M.; Lim, S. Assessment of earthquake-induced landslide inventories and susceptibility maps using slope unit-based logistic regression and geospatial statistics. *Sci. Rep.* **2021**, *11*, 21333. [CrossRef]

19. Zhang, S.; Wang, Y.; Wu, G. Earthquake-Induced Landslide Susceptibility Assessment Using a Novel Model Based on Gradient Boosting Machine Learning and Class Balancing Methods. *Remote Sens.* **2022**, *14*, 5945. [CrossRef]
20. Koukouvelas, I.K.; Nikolakopoulos, K.G.; Zygouri, V.; Kyriou, A. Post-seismic monitoring of cliff mass wasting using an unmanned aerial vehicle and field data at Egremni, Lefkada Island, Greece. *Geomorphology* **2020**, *367*, 107306. [CrossRef]
21. Nikolakopoulos, K.; Kyriou, A.; Koukouvelas, I.; Zygouri, V.; Apostolopoulos, D. Combination of Aerial, Satellite, and UAV Photogrammetry for Mapping the Diachronic Coastline Evolution: The Case of Lefkada Island. *ISPRS Int. J. Geo-Inf.* **2019**, *8*, 489. [CrossRef]
22. Båth, M. The seismology of Greece. *Tectonophysics* **1983**, *98*, 165–208. [CrossRef]
23. Caputo, R.; Chatzipetros, A.; Pavlides, S.; Sboras, S. The Greek Database of Seismogenic Sources (GreDaSS): State-of-the-art for northern Greece. *Ann. Geophys.* **2013**, *55*, 859–894. [CrossRef]
24. Karakostas, V.; Papadimitriou, E.; Patias, P.; Georgiadis, C. Coastal deformation in Lefkada Island associated with strong earthquake occurrence. *Boll. Di Geofis. Teor. Ed Appl.* **2019**, *60*, 1–16. [CrossRef]
25. Hatzfeld, D.; Kassaras, I.; Panagiotopoulos, D.; Amorese, D.; Makropoulos, K.; Karakaisis, G.; Coutant, O. Microseismicity and strain pattern in northwestern Greece. *Tectonics* **1995**, *14*, 773–785. [CrossRef]
26. Ganas, A.; Marinou, A.; Anastasiou, D.; Paradissis, D.; Papazissi, K.; Tzavaras, P.; Drakatos, G. GPS-derived estimates of crustal deformation in the central and north Ionian Sea, Greece: 3-yr results from NOANET continuous network data. *J. Geod.* **2013**, *6*, 62–71.
27. Clement, C.; Hirn, A.; Charvis, P. Seismic structure and the active Hellenic subduction in the Ionian islands. *Tectonics* **2000**, *329*, 141–156. [CrossRef]
28. Louvari, E.; Kiratzi, A.; Papazachos, B. The Cephalonia Transform Fault and its extension to western Lefkada Island (Greece). *Tectonophysics* **1999**, *308*, 223–236. [CrossRef]
29. Kokinou, E.; Papadimitriou, E.; Karakostas, V.; Kamberis, E.; Vallianatos, F. The Kefalonia Transform Zone (offshore Western Greece) with special emphasis to its prolongation towards the Ionian Abyssal Plain. *Mar. Geophys. Res.* **2006**, *27*, 241–252. [CrossRef]
30. Kokkalas, S.; Xypolias, P.; Koukouvelas, I.K.; Doutsos, T. Post-Collisional Contractional and Extensional Deformation in the Aegean Region. In *Post-Collisional Tectonics and Magmatism in the Mediterranean region and Asia*; Dilek, Y., Pavlides, S., Eds.; Geological Society of America Special Paper; The Geological Society of America: Boulder, CO, USA, 2006; Volume 409, pp. 97–123.
31. Papadopoulos, G.A.; Plessa, A. Magnitude-distance relations for earthquake-induced landslides in Greece. *Eng. Geol.* **2000**, *58*, 377–386. [CrossRef]
32. Bornovas, J. Géologie de l' île de Lefkade. *Geol. Geophys. Res.* **1964**, *10*, 142.
33. Cushing, M. Evolution Structurale de la Marge Nord-Ouest Hellénique Dans l'île de Lefkas et ses Environs (Grèce Nord-Occidentale). Ph.D. Thesis, Univ. d' Orsay, Orsay, France, 1985.
34. Karakostas, V.G. Properties of the 2003 Lefkada, Ionian Islands, Greece, Earthquake Seismic Sequence and Seismicity Triggering. *Bull. Seismol. Soc. Am.* **2004**, *94*, 1976–1981. [CrossRef]
35. Zahradnik, J.; Serpetsidaki, A.; Sokos, E.; Tselentis, G.-A. Iterative Deconvolution of Regional Waveforms and a Double-Event Interpretation of the 2003 Lefkada Earthquake, Greece. *Bull. Seismol. Soc. Am.* **2005**, *95*, 159–172. [CrossRef]
36. Benetatos, C.; Dreger, D.; Kiratzi, A. Complex and Segmented Rupture Associated with the 14 August 2003 Mw 6.2 Lefkada, Ionian Islands, Earthquake. *Bull. Seismol. Soc. Am.* **2007**, *97*, 35–51. [CrossRef]
37. Sokos, E.; Zahradník, J.; Gallovic, F.; Serpetsidaki, A.; Plicka, V.; Kiratzi, A. Asperity break after 12 years: The Mw6.4 2015 Lefkada (Greece) earthquake. *Geophys. Res. Lett.* **2016**, *43*, 6137–6145. [CrossRef]
38. Ganas, A.; Elias, P.; Bozionelos, G.; Papathanassiou, G.; Avallone, A.; Papastergios, A.; Valkaniotis, S.; Parcharidis, I.; Briole, P. Coseismic deformation, field observations and seismic fault of the 17 November 2015 M = 6.5, Lefkada Island, Greece earthquake. *Tectonophysics* **2016**, *687*, 210–222. [CrossRef]
39. Bie, L.; González, P.J.; Rietbrock, A. Slip distribution of the 2015 Lefkada earthquake and its implications for fault segmentation. *Geoph. Jour. Int.* **2017**, *210*, 420–427. [CrossRef]
40. Chousianitis, K.; Konca, A.O.; Tselentis, G.A.; Papadopoulos, G.A.; Gianniou, M. Slip model of the 17 November 2015 Mw =6.5 Lefkada earthquake from the joint inversion of geodetic and seismic data. *Geophys. Res. Lett.* **2016**, *43*, 7973–7981. [CrossRef]
41. Melgar, D.; Ganas, A.; Geng, J.; Liang, C.; Fielding, E.J.; Kassaras, I. Source characteristics of the 2015 Mw6.5Lefkada, Greece, strike-slip earthquake. *J. Geophys. Res. Solid Earth* **2017**, *122*, 2260–2273.
42. Svigkas, N.; Atzori, S.; Kiratzi, A.; Tolomei, C.; Antonioli, A.; Papoutsis, I.; Salvi, S.; Kontoes, C. On the Segmentation of the Cephalonia–Lefkada Transform Fault Zone (Greece) from an InSAR Multi-Mode Dataset of the Lefkada 2015 Sequence. *Remote Sens.* **2019**, *11*, 1848. [CrossRef]
43. Papathanassiou, G.; Valkaniotis, S.; Ganas, A.; Grendas, N.; Kollia, E. The November 17th, 2015 Lefkada (Greece) strike-slip earthquake: Field mapping of generated failures and assessment of macroseismic intensity ESI-07. *Eng. Geol.* **2015**, *220*, 13–30. [CrossRef]
44. Kassaras, I.; Kazantzidou-Firtinidou, D.; Ganas, A.; Tonna, S.; Pomonis, A.; Karakostas, C.; Papadatou-Giannopoulou, C.; Psarris, D.; Lekkas, E.; Makropoulos, K. On the Lefkas (Ionian Sea) November 17, 2015 Mw = 6.5 Earthquake Macroseismic Effects. *J. Earthq. Eng.* **2018**, *24*, 1913–1943. [CrossRef]

45. Lekkas, E.; Mavroulis, S.; Carydis, P.; Alexoudi, V. The 17 November 2015 Mw 6.4 Lefkas (Ionian Sea, Western Greece) Earthquake: Impact on Environment and Buildings. *Geotech. Geol. Eng.* **2018**, *36*, 2109–2142. [CrossRef]
46. Polykretis, C.; Kalogeropoulos, K.; Andreopoulos, P.; Faka, A.; Tsatsaris, A.; Chalkias, C. Comparison of Statistical Analysis Models for Susceptibility Assessment of Earthquake-Triggered Landslides: A Case Study from 2015 Earthquake in Lefkada Island. *Geosciences* **2019**, *9*, 350. [CrossRef]
47. Servou, A.; Vagenas, N.; Depountis, N.; Roumelioti, Z.; Sokos, E.; Sabatakakis, N. Rockfall Intensity under Seismic and Aseismic Conditions: The Case of Lefkada Island, Greece. *Land* **2023**, *12*, 172. [CrossRef]
48. Tsangaratos, P.; Loupasakis, C.; Nikolakopoulos, K.G.; Angelitsa, V.; Ilia, I. Developing a landslide susceptibility map based on remote sensing, fuzzy logic and expert knowledge of the Island of Lefkada, Greece. *Environ. Earth Sci.* **2018**, *77*, 1–23.
49. Nikolakopoulos, K.G.; Soura, K.; Koukouvelas, I.K.; Argyropoulos, N.G. UAV vs classical aerial photogrammetry for archaeological studies. *J. Archaeol. Sci. Rep.* **2017**, *14*, 758–773. [CrossRef]
50. Rice, R.M. Sedimentation in the chaparral: How do you handle unusual events? In *Sediment Budgets and Routing in Forested Drainage Basins*; Swanson, F.J., Ed.; U.S. Department of Agriculture: Washington, DC, USA, 1982; pp. 39–49.
51. Gabet, E.J. Sediment transport by dry ravel. *J. Geophys. Res.* **2003**, *108*, 2049. [CrossRef]
52. Yang, X.; Chen, L. Using multi-temporal remote sensor imagery to detect earthquake-triggered landslides. *Int. J. Appl. Earth Obs. Geoinf.* **2010**, *12*, 487–495. [CrossRef]
53. Xu, C. Preparation of earthquake-triggered landslide inventory maps using remote sensing and GIS technologies: Principles and case studies. *Geosci. Front.* **2015**, *6*, 825–836. [CrossRef]
54. Huang, Y.; Zhang, J.; Zhang, L.; Ming, Z.; He, H.; Chen, R.; Ge, Y.; Liu, R. How Spatial Resolution of Remote Sensing Image Affects Earthquake Triggered Landslide Detection: An Example from 2022 Luding Earthquake, Sichuan, China. *Land* **2023**, *12*, 681. [CrossRef]
55. Liu, W.; Yamazaki, F. Detection of landslides due to the 2013 Thypoon Wipha from high-resolution airborne SAR images. In Proceedings of the 2015 IEEE International Geoscience and Remote Sensing Symposium (IGARSS), Milan, Italy, 26–31 July 2015; pp. 4244–4247. [CrossRef]
56. Plank, S.; Twele, A.; Martinis, S. Landslide Mapping in Vegetated Areas Using Change Detection Based on Optical and Polarimetric SAR Data. *Remote Sens.* **2016**, *8*, 307. [CrossRef]
57. Wu, B.S.; Chuang, R.Y.; Chen, Y.C. Characteristics of landslides triggered by the 2013 ML6.5 Nantou, Taiwan, earthquake. *Earth Planets Space* **2022**, *74*, 7. [CrossRef]
58. Hapke, C.; Richmond, B. The impact of climatic and seismic events on the short-term evolution of seacliffs based on 3-D mapping: Northern Monterey Bay, California. *Mar. Geol.* **2002**, *187*, 259–278. [CrossRef]
59. Zhou, Y.; Parsons, B.; Elliott, J.R.; Barisin, I.; Walker, R.T. Assessing the ability of Pleiades stereo imagery to determine height changes in earthquakes: A case study for the El Mayor-Cucapah epicentral area. *J. Geophys. Res. Solid Earth* **2015**, *120*, 8793–8808. [CrossRef]
60. Bloom, C.K.; Singeisen, C.; Stahl, T.; Howell, A.; Massey, C. Earthquake Contributions to Coastal Cliff Retreat. *EGUsphere* **2022**. [CrossRef]
61. Naylor, L.A.; Stephenson, W.J.; Trenhaile, A.S. Rock coast geomorphology: Recent advances and future reasearch directions. *Geomorphology* **2009**, *114*, 3–11. [CrossRef]
62. Griggs, G.; Plant, N. Coastal-bluff failures in northern Monterey Bay induced by the earthquake. In *The Loma Prieta, California, Earthqukae of October 17, 1989*; Landslides US Geological Survey Professional Paper; Government Printing Office: Washington, DC, USA, 1998; Volume 1551–C, pp. 51–70.
63. Gallousi, C.; Koukouvelas, I.K. Quantifying geomorphic evolution of earthquake-triggered landslides and their relation to active normal faults. An example from the Gulf of Corinth, Greece. *Tectonophysics* **2007**, *440*, 85–104. [CrossRef]
64. Keefer, D.K. Landslides caused by earthquakes. *Bull. Geol. Soc. Am.* **1984**, *95*, 406–421. [CrossRef]
65. Sørensen, M.B.; Haga, T.; Nesje, A. Earthquake-induced landslides in Norway. *Nat. Hazards Earth Syst. Sci.* **2023**, *23*, 1577–1592. [CrossRef]
66. Wistuba, M.; Malik, I.; Krzemień, K.; Gorczyca, E.; Sobucki, M.; Wrońska-Wałach, D.; Gawior, D. Can low-magnitude earthquakes act as a triggering factor for landslide activity? Examples from the Western Carpathian Mts, Poland. *Catena* **2018**, *171*, 359–375. [CrossRef]
67. Koukouvelas, I.; Mpresiakas, A.; Sokos, E.; Doutsos, T. The tectonic setting and earthquake hazards of the 1993 Pyrgos earthquake, Peloponnese, Greece. *J. Geol. Soc. Lond.* **1996**, *153*, 39–49. [CrossRef]